ADVANCED MATERIALS

Supporting Information

for *Adv. Mater.*, DOI 10.1002/adma.202312590

Integrating Light Diffusion and Conversion Layers for Highly Efficient Multicolored Fiber-Dye-Sensitized Solar Cells

Jiatian Song, Yu Gu, Zhengmeng Lin, Jiuzhou Liu, Xinyue Kang, Xiaocheng Gong, Peiyu Liu, Yiqing Yang, Hongyu Jiang, Jiaqi Wang, Siwei Cao, Zhengfeng Zhu and Huisheng Peng**

Supporting Information for

Integrating Light Diffusion and Conversion Layers for Highly Efficient Multi-Colored Fiber Dye-Sensitized Solar Cells

Jiatian Song, Yu Gu, Zhengmeng Lin, Jiuzhou Liu, Xinyue Kang, Xiaocheng Gong, Peiyu Liu, Yiqing Yang, Hongyu Jiang, Jiaqi Wang, Siwei Cao, Zhengfeng Zhu, and Huisheng Peng**

J. Song, Z. Lin, J. Liu, X. Kang, X. Gong, P. Liu, Y. Yang, H. Jiang, J. Wang, S. Cao, Dr. Z. Zhu, Prof. H. Peng
State Key Laboratory of Molecular Engineering of Polymers, Department of Macromolecular Science, and Institute of Fiber Materials and Devices, Fudan University, Shanghai 200438, China.

Prof. Y. Gu
Key Laboratory of Advanced Display Materials and Devices, Ministry of Industry and Information Technology, Institute of Optoelectronics & Nanomaterials, College of Material Science and Engineering, Nanjing University of Science and Technology, Nanjing 210094, China.

Corresponding Email: zhuzf@fudan.edu.cn; penghs@fudan.edu.cn.

This file includes:

Materials and Methods

All materials, including commercial titanium wire (metal basis: 99.9%, diameter: 50/150 μm), titanium oxide (anatase, metal basis: 99.8%, size: 200–400 nm, Aladdin), ultraviolet /near-infrared excited phosphors (Color Chang Technology Co., Ltd.), aluminum oxide (size: 1–3 μm, Zhejiang Yuante New Material Co., Ltd.), yellow gouache pigments (Lemon Yellow 215, G1100, Shanghai Marie Painting MATERIALS), green gouache pigments (Green Mid 505, G1100, Shanghai Marie Painting MATERIALS), blue gouache pigments (Sky Blue 447, G1100, Shanghai Marie Painting MATERIALS), red gouache pigments (Scarlet 302, G1100, Shanghai Marie Painting MATERIALS), poly(vinylidene fluoride-co-hexafluoropropylene) (pellets, Sigma-Aldrich), aqueous polyurethane emulsion (U-9, 50%, Laoling Sisheng Polymer Materials Co., Ltd.), iodine (99.8%, J&K), lithium iodide (anhydrous, 98.5%, J&K), 1,2-dimethyl-3-propylimidazolium iodide (98%, TCI), 4-tert-butylpyridine (96%, Aladdin), ammonium fluoride (metal basis: 99.99%, Aladdin), ethylene glycol (99.5%, Sinopharm), ethanol (99.7%, Sinopharm), tert-butyl alcohol (99%, Aladdin), N,N-Dimethylformamide (99.5%, Sinopharm), acetonitrile (98%, Aladdin), acetone (99.5%, Sinopharm), isopropanol (99.7%, Sinopharm), valinomycin (Sigma), sodium tetrakis[3,5-bis(trifluoromethyl)phenyl] borate (98%, Sigma), dioctyl sebacate (Sigma), tetrahydrofuran (≥97.0%, Aladdin), poly(3,4-ethylenedioxythiophene)-poly(styrenesulfonate) (Aladdin), N719 dye (HPLC:90%, Aladdin) and heat-shrinking tubes (Zhongshan Wolida Electronic Material Co., Ltd.) were commercially available and used without further treatment unless otherwise mentioned.

1. Preparation of fiber photoanodes

TiO_2 nanotube arrays were prepared on titanium wires by an anodization process. After Ti wire was cleaned with acetone, isopropyl alcohol and deionized water, it was anodized in a glycol solution containing 3.3 g/L NH_4F and 88 g/L H_2O at 60 V and 40 °C for 6 h, and then washed with deionized water. The anodized Ti wire was annealed in a tube furnace, starting from room temperature, at a heating rate of 8 °C/ min to 500 °C, and held for 1 h. N719 dye solution was prepared by dissolving 0.3 mM N719 dyes in tert-butanol/acetonitrile (1/1, v/v). The cooled Ti wire with TiO_2 layer was soaked in the dye solution for 36 h to obtain the fiber photoanode.

2. Preparation of light diffusion layer

10 wt% Al_2O_3 was mixed with PU aqueous solution by ball milling for 1 h to obtain Al_2O_3 /PU slurry. Then the slurry was coated on a transparent tube and dried in air to achieve a light diffusion layer.

3. Preparation of hybrid counter electrode with light conversion layer

An aligned CNT sheet was prepared by floating catalyst chemical vapor deposition. The feed solution was composed of ethanol as carbon source, 2.5 wt% ferrocene and 2 wt% thiophene as composite catalysts. The solution was placed in a hydrogen and argon atmosphere at 1200 °C at a flow rate of 0.2 mL/min. The synthesized CNTs were removed from the furnace, densified by water, and dried in air to form an aligned CNT sheet. Then, the CNT sheet was closely wrapped on a Ti wire at a specific angle to construct a Ti/CNT fiber. After P(VDF-HFP) and TiO_2 nanoparticles were dispersed in DMF with a content of 24.44 wt% by stirring for 4 h at 70 °C, CNT/Ti fiber was dip-coated with TiO_2/P(VDF-HFP) slurry and soaked in water for 20 min, followed by air drying at 80 °C to obtain TiO_2/P(VDF-HFP) film. Then UV/NIR excited phosphor were dispersed in DMF solution containing 20 wt% P(VDF-HFP) by stirring for 4 h at 70 °C. The above functional fiber was further dip-coated with phosphor/P(VDF-HFP) slurry and soaked in water for 20 min, followed by air drying at 80 °C for a light conversion layer. Finally, the hybrid fiber counter electrode was obtained.

4. Fabrication of FDSSCs

An electrolyte was prepared by dissolving 6 mM I_2, 0.1 M LiI, 0.6 M 1,2-dimethyl-3-propylimidazolium iodide, and 1 M 4-tert-butylpyridine in acetonitrile. Then, the as-prepared fiber photoanode and hybrid counter electrode with light conversion layer were encapsulated in a transparent tube covered with light diffusion layer, followed by injecting electrolyte to produce the FDSSC.

5. Preparation of multicolored light diffusion layers.

10 wt% Al_2O_3 particles and 0.02 wt% pigment were mixed with PU aqueous solution

by ball milling for 1 h to obtain multicolored slurry. Then the slurry was coated on a transparent tube and dried in air to achieve multicolored light diffusion layers.

6. Fabrication of fiber lithium-ion batteries

A fiber positive electrode was prepared by dip-coating a positive slurry (lithium cobalt oxide, super-P, polyvinylidene fluoride, N-methyl-2-pyrrolidone) on an Al wire (diameter of 200 μm). A fiber negative electrode was prepared by dip-coating a negative slurry (graphite, super-P, sodium carboxymethyl cellulose, butadiene styrene rubber, water) on a Cu wire (diameter of 200 μm). The two fiber electrodes were then wrapped with separator strips. The above electrodes were twisted and encapsulated in a tube with injected electrolyte.

7. Fabrication of textile display modules

The textile display module was fabricated by weaving electroluminescent yarns into textiles. The electroluminescent yarn was made by coating the conductive yarn with a layer of electroluminescent paste composed of waterborne polyurethane dispersed with 75 wt% ZnS phosphors and then a layer of insulating paste, and finally twisted with a conducting wire.

8. Fabrication of fiber biosensors

For fabrication of K^+ sensing fibers, the K^+-selective membrane cocktail was prepared by mixing 4.2 mg valinomycin, 68.6 mg polyvinyl chloride, 1.1 mg sodium tetrakis[3,5-bis(trifluoromethyl)phenyl] borate, and 129.2 mg dioctyl sebacate into 2.4 mL tetrahydrofuran. Poly(3,4-ethylenedioxythiophene)–poly(styrenesulfonate) was dip-coated onto the surface of CNT fiber. Then, the treated CNT fiber was dried at room temperature overnight. Then, 4 μL of the ion-selective membrane solution was coated onto the fiber. The fabricated fiber biosensors were stored at 4 °C before use.

9. Characterization

J-V curves of FDSSCs were measured with a source meter (Keithley 2420) from 0.9 to −0.2 V with a dwell time of 50 ms under simulated AM 1.5G sunlight by a solar simulator (Newport 94023A). Transmittance and haze of light diffusion layer,

absorption spectra of dye solutions and reflectance of reflective light conversion layer were measured by a UV-visible spectrophotometer (Lambda 750, Perkin Elmer). Excitation and emission spectra of phosphor and reflective light conversion layer were measured by a high-resolution fluorescence spectrometer (FLS1000, Edinburgh). Photoluminescence quantum yield (PLQY) of phosphors was measured by a high-resolution fluorescence spectrometer (FLS1000, Edinburgh) and an integrating sphere accessory. Scanning electron microscopy (SEM) images were obtained by a field-emission scanning electron microscope (Zeiss Sigma, operated at 3 kV). X-ray photoelectron spectroscopy (XPS) spectra were measured by an X-ray Photoelectron Spectrometer (Thermo Scientific ESCALAB Xi+) with Al Kα radiation as the X-ray source. Power X-ray Diffraction (XRD) patterns were measured by an X-ray diffractometer (Rigaku D/max-2200PC) at 5°/min over the range of 10−80° (2θ). Incident photon-to-current conversion efficiency (IPCE) spectra were measured by an external quantum efficiency (EQE) measurement system containing a power meter (2936-R, Newport) and a monochromator (Cornerstone 260-74125, Newport). Electrochemical impedance spectra (EIS) were measured by an electrochemical workstation (CHI 660E, Shanghai Chenhua). The wearable ECG sensor involved is a common commercial product that is operated strictly in accordance with the product instructions. The human experiments conformed to the regulation of the Animal and Human Experimentation Committee of Fudan University. A healthy subject from Fudan University had provided written informed consent before participating in the study.

10. Calculation of PCEs of FDSSCs.

According to the standard calculation method,[48-50] the effective area of FDSSC was represented by the projected area of the photoanode, calculated from its effective length and average diameter. The PCE of FDSSCs was calculated by the following equations:

$$PCE = \frac{I_{SC} \times V_{OC} \times FF}{A \times P_{in}} \quad \text{(S1)}$$

$$A = d \times l \quad \text{(S2)}$$

where I_{SC} is the short-circuit current, P_{in} is the power density of incident light, A is the projected area of the photoanode, d is the average diameter of the photoanode, and l is the effective length of the photoanode.

11. Calculation of haze of light diffusion layer.

From ultraviolet-visible transmission spectrum of light diffusion layer, haze was calculated by the following equations according to GB/T 2410-2008:

$$Haze = \frac{T_d}{T_t} \times 100\% \quad \text{(S3)}$$

where T_t is the light transmittance of the light diffusion layer, and T_d is the transmittance of the light that deviates from the incident light by more than 2.5°.

12. Calculation of PLQY of UV/NIR excited phosphors

The photoluminescence quantum yield (PLQY) was directly measured by integrating sphere method.[51-53] The inner surface of the sphere shell was coated with a material with total reflection characteristics, which can capture the light entering and leaving the sphere. The fluorescence emission (E_c) and scattering (L_c) of the sample and the emission (E_a) and scattering (L_a) of the blank cavity were obtained by measuring the spectra of the sample and the blank cavity, respectively. Then the PLQY could be calculated by the following equations:

$$\text{PLQY} = \frac{E_c - (1-A)E_b}{L_a \cdot A} = \frac{E_c - E_a}{L_a - L_c} \quad \text{(S4)}$$

where E_b is the fluorescence integral of the sample according to indirect luminescence from the integrating sphere, and A is the absorption value of the sample at the excitation wavelength.

13. Simulation of optical fields

The optical simulation follows the standard Monte Carlo simulation for photon transport with a slight revision. Since we intend to show the field distribution in the transparent area (no absorption, no scattering), the trajectory of each individual photon was recorded and photon weight was dropped to every bin along its trace until it was absorbed by the structure or escaped from the structure. A total of 10^6 photons were launched from the top half of the enclosing circle in each simulation. If the encapsulating diffuse layer was not present, collimated photons were launched. Otherwise, the photons were launched diffusively. The surface of the counter-electrode was treated as either a perfect absorbing surface or a perfect diffuse

reflection surface. The photoanode always absorbed photon perfectly. The normalized optical field distribution I is defined as:

$$I(i,j) = \frac{N(i,j)}{10^6/N_L} \quad \text{(S5)}$$

where i, j are the index of the bins to record the trace of photons, respectively, $N(i, j)$ is the total number of photons that is accumulated in the bin (i, j), and N_L is the total number of bins for launching photons.

14. Calculation of light conversion efficiency

Integrated current density ($J_{SC,INT}$) can be calculated according to IPCE spectra by the following equation:

$$J_{SC,INT} = \int_{\lambda 2}^{\lambda 1} F(\lambda) IPCE(\lambda) d\lambda \quad \text{(S6)}$$

where $F(\lambda)$ is photon flux at AM 1.5G.

Light conversion efficiency can be calculated by the following equation:

$$Light\ conversion\ efficiency(\%) = \frac{J_{SC,INT}(A)}{J_{SC,INT}(B)} \times 100\% \quad \text{(S7)}$$

where $J_{SC,INT}$(A) is the actual integrated current density obtained by FDSSC, and $J_{SC,INT}$(B) is the ideal integrated current density when solar spectrum is converted by 100%.

The ideal integrated current densities ($J_{SC,INT}$) according to solar spectrum were 1.54 mA/cm^2 and 19.43 mA/cm^2 in 300−400 nm and 800−1100 nm wavelength ranges, respectively. According to the IPCE spectra in Figure S21 and Equation S6, the increased values of integrated current densities ($J_{SC,INT}$) obtained by FDSSC with diffusion and conversion layers were 0.43 mA/cm^2 and 2.56 mA/cm^2 in 300−400 nm and 800−1100 nm wavelength ranges, respectively. Taking above values into Equation S7, the conversion efficiencies when converting UV and NIR light into wavelengths that overlap with the absorption spectrum of the active N719 dye in 300−1100 nm wavelength range were calculated as 27.92% and 13.18%, respectively.

15. Outdoor testing

All tests were conducted at the same time and place. The tests that took place on December 24, 2023 in Yangpu District, Shanghai, China (longitude: 121.51, latitude:

31.34) were used to evaluate the photovoltaic performance of FDSSCs under real sunlight compared with that measured in the lab. Irradiation intensities of sunlight were determined by the illuminance values measured by a digital illuminometer (DL333215, Deli). For the measurement of long-term stability of FDSSCs under solar exposure, they were placed outdoors in Yangpu District, Shanghai, China (longitude: 121.51, latitude: 31.34) and in a sealed glass box that can be filled with argon.

16. Statistical analysis

The thickness of light conversion layer was defined as half of the difference value between the average dimeters of fiber counter electrodes before and after dip-coating phosphor slurry. PCE value of FDSSCs for comparison was presented as the mean ± standard deviation of five measured FDSSCs at least. The PCE variation was defined as the standard deviation of PCE divided by its average value.

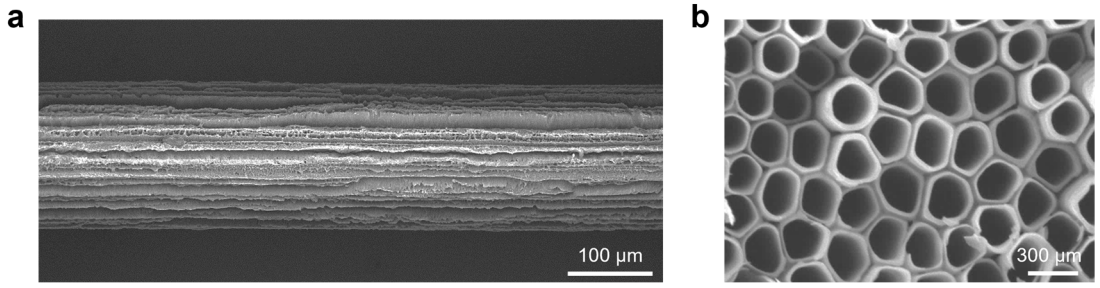

Figure S1. a) SEM image of fiber photoanode. b) High-resolution SEM image of the fiber photoanode with TiO_2 nanotube array.

Figure S2. Photograph of the FDSSC partly covered with light diffusion layer. The light diffusion layer gives the solar cell a white appearance, which can effectively hide the internal electrode structure and achieve visual integration.

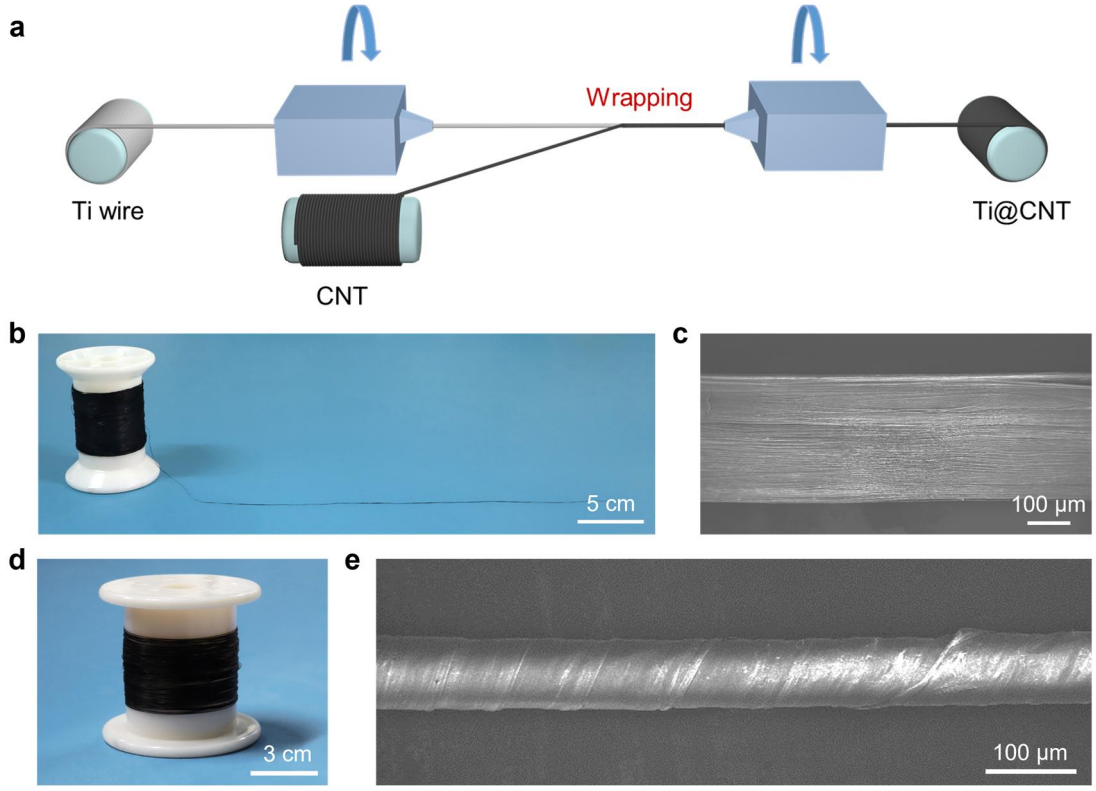

Figure S3. a) Diagram illustrating the preparation flow of Ti/CNT fiber. An aligned CNT sheet was closely wrapped around Ti wire. b) Photograph of a reel of CNT sheet synthesized by floating catalyst chemical vapor deposition. c) SEM image of the aligned CNT sheet. d) Photograph of a reel of Ti/CNT fiber. e) SEM image of Ti/CNT fiber.

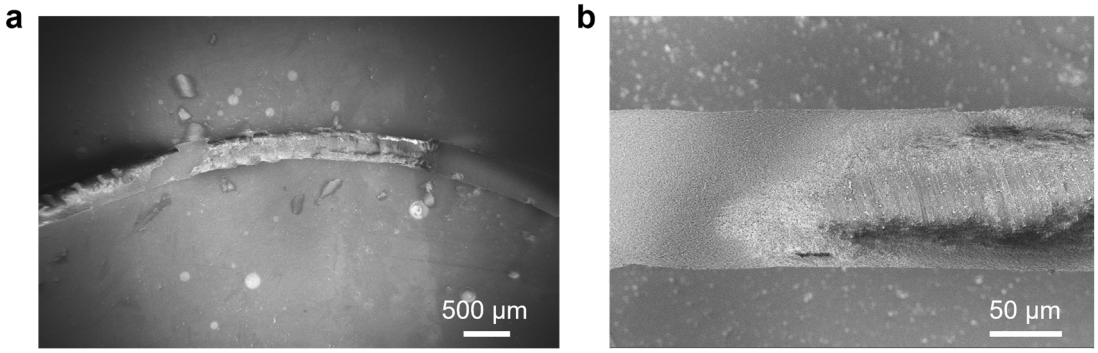

Figure S4. a) SEM image of bare phosphor film on Ti/CNT fiber under bending at curvature radius of 1.2 cm. b) Magnified SEM image of (a). The pure phosphor film was not uniform and may easily peel off the Ti/CNT surface.

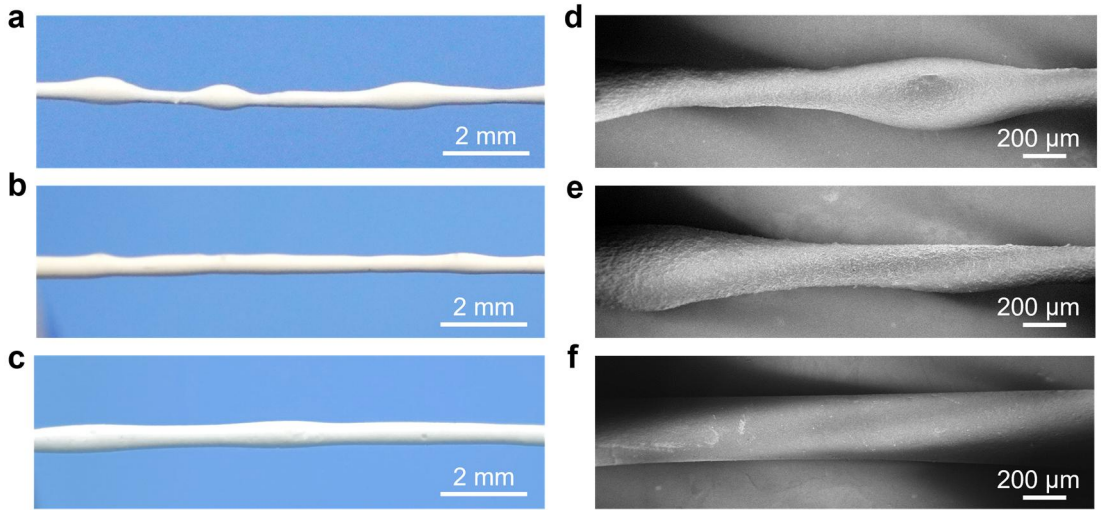

Figure S5. a–c) Photographs of fiber counter electrodes after dip-coating with the as-prepared phosphor/P(VDF-HFP) slurries with P(VDF-HFP) contents of 2.44 wt%, 4.56 wt%, and 7.00 wt% with slurry viscosities of 1.90, 6.20, and 12.23 Pa·s, respectively. d–f) Corresponding SEM images in (a–c). The slurry with low viscosity produced bead-like aggregates on fibers. The increasing concentration of P(VDF-HFP) effectively enhanced the viscosity of the slurry to overcome its surface tension, but high viscosity would also easily make excessive slurry adhere to fiber surfaces and form irregular aggregates under gravity.

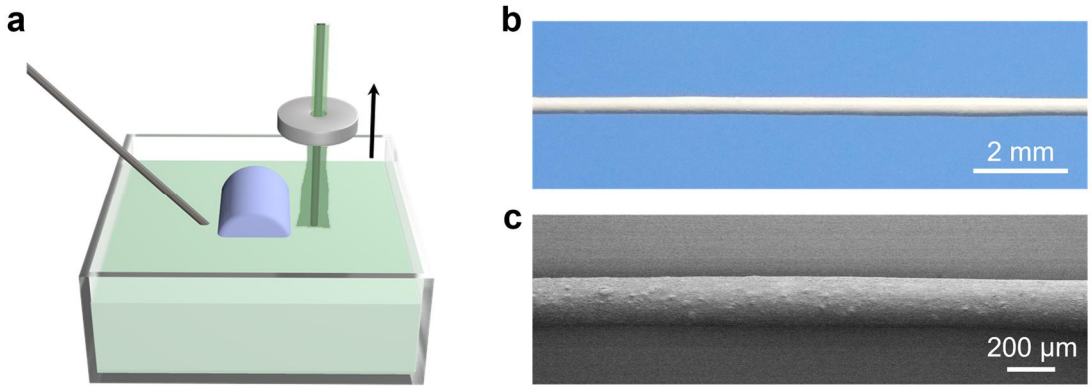

Figure S6. a) Schematic diagram illustrating the process of a pinhole scraper to exclude the superfluous slurry on fibers. b, c) Photograph and corresponding SEM image of fiber counter electrode after dip-coating by pinhole scraper with the slurries with P(VDF-HFP) contents of 7.00 wt%, respectively. The pinhole scraper effectively excluded superfluous slurry to produce uniform phosphor/P(VDF-HFP) film on fiber.

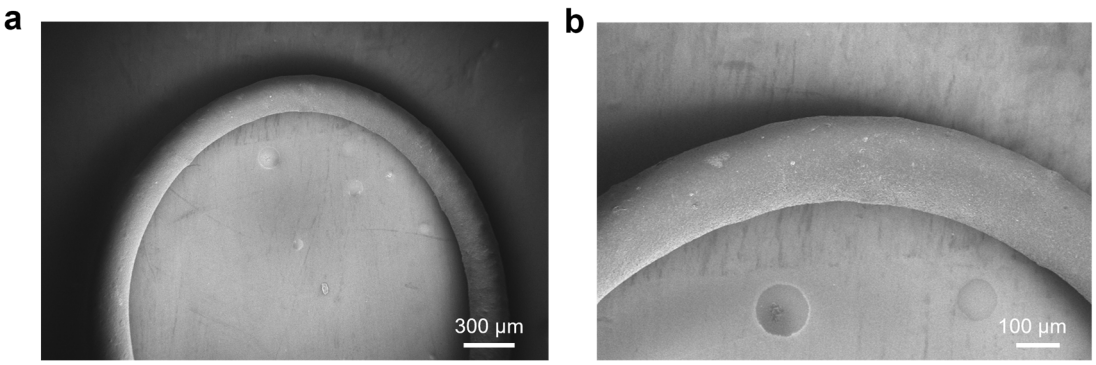

Figure S7. a) SEM image of a bent fiber counter electrode after dip-coating with the as-prepared phosphors/ P(VDF-HFP) slurry with P(VDF-HFP) contents of 7.00 wt% (curvature radius of 1.6 mm). b) Magnified SEM image of (a). The film with P(VDF-HFP) was tightly attached to the Ti/CNT surface and would not peel off.

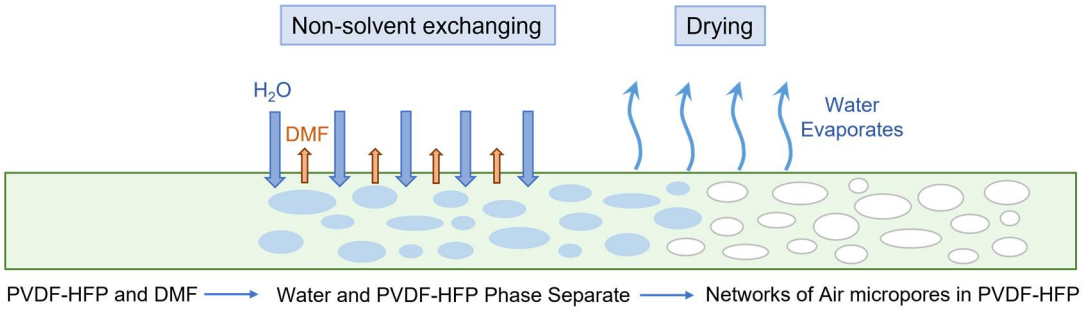

Figure S8. Schematic of the non-solvent exchanging process, showing the formation of a hierarchically porous polymer coating from a solution of DMF (solvent), water (non-solvent), and P(VDF-HFP) (polymer).

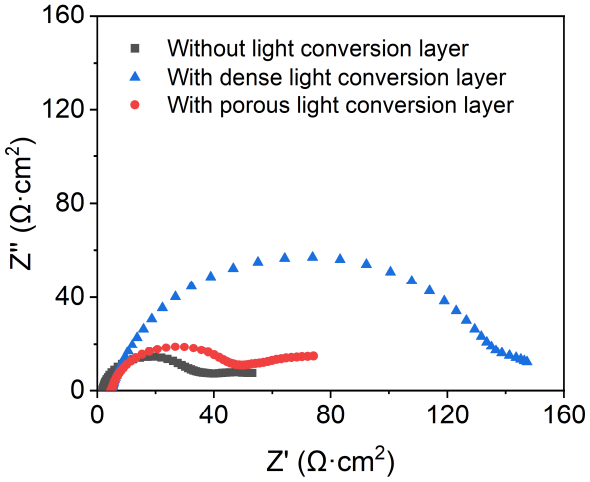

Figure S9. a) Nyquist plots of symmetrical cells fabricated with two identical electrodes measured at 0 V from 100 kHz to 0.01 Hz in 3-methoxypropionitrile solution containing 6 mM I_2, 0.1 M LiI, 0.6 M 1,2-dimethyl-3-propylimidazolium iodide, and 1 M 4-tert-butylpyridine. Inset, enlarged view of Nyquist plots at high frequency. The corresponding series resistance (R_S), charge transfer resistances (R_{CT}), and Nernst diffusion resistance (Z_N) of fiber counter electrode without light conversion layer were 1.76, 0.30 and 33.40 Ω·cm^2, respectively, while R_S, R_{CT}, and Z_N of fiber counter electrode with dense light conversion layer were 4.43, 0.63, and 144.71 Ω·cm^2, respectively, showing obviously higher Z_N values which seriously hindered the diffusion of electrolyte. R_S, R_{CT}, and Z_N of fiber counter electrode with porous light conversion layer were 4.53, 0.73, and 45.99 Ω·cm^2, respectively, only showing slightly higher R_S and Z_N values than those without light conversion layer, which also accounted for their high PCEs.

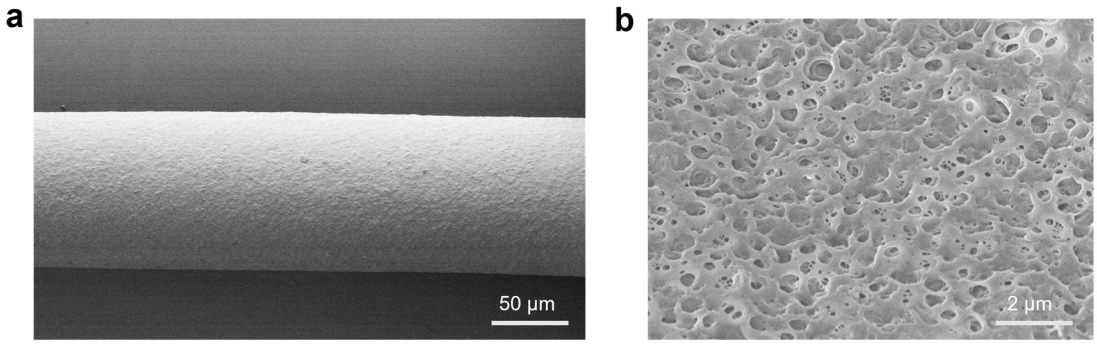

Figure S10. a) SEM image of TiO_2/P(VDF-HFP) film with 10 µm on Ti/CNT fiber fiber. b) Magnified SEM image of TiO_2/P(VDF-HFP) film, showing a porous structure.

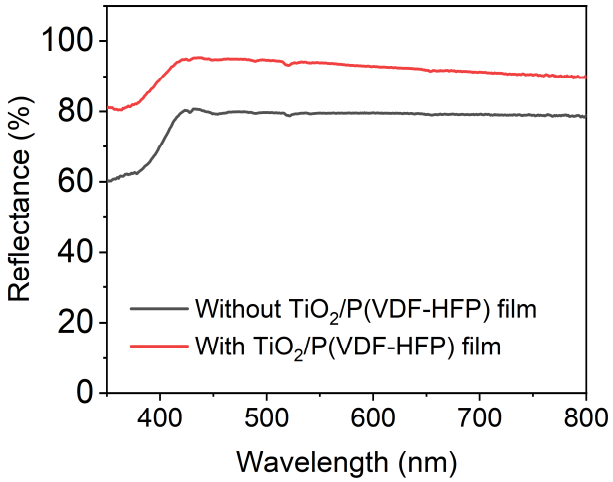

Figure S11. Reflectance spectra of the light conversion layer with and without TiO_2/P(VDF-HFP) film.

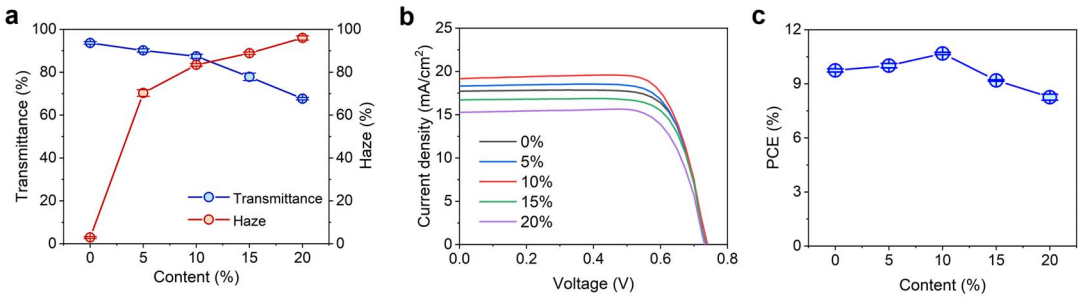

Figure S12. a) Average light transmittance and haze of light diffusion layers with different Al_2O_3 contents at wavelengths of 300−1200 nm. Error bars, standard deviations of the results from five samples. b) Corresponding *J-V* curves of FDSSCs using light diffusion layers with different Al_2O_3 contents. c) PCE values of FDSSCs using light diffusion layers with different Al_2O_3 contents. Error bars, standard deviations of the results from five samples.

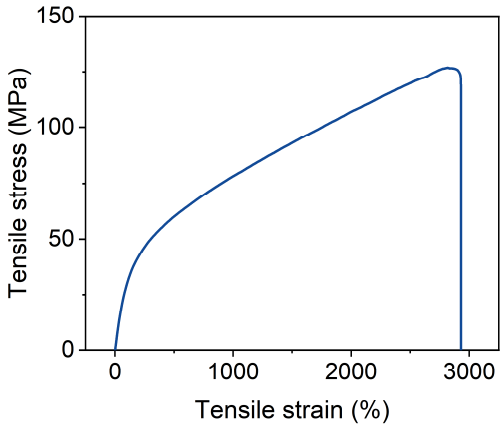

Figure S13. Stress–strain behavior of Al_2O_3/PU film. The tensile strength was 126.8 MPa and the elongation at breaking was 2927.6%.

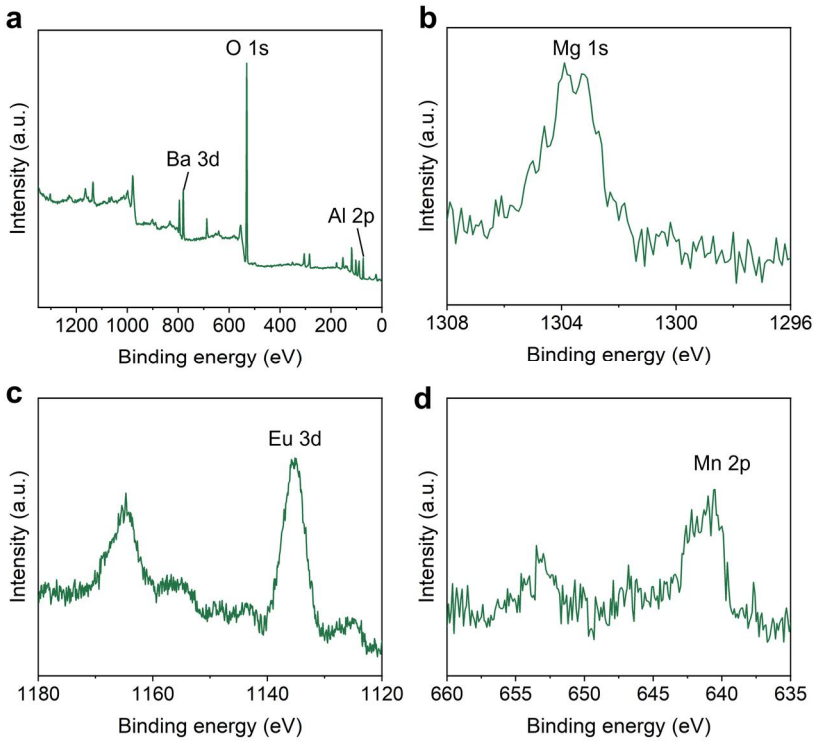

Figure S14. XPS spectra of UV excited phosphor.

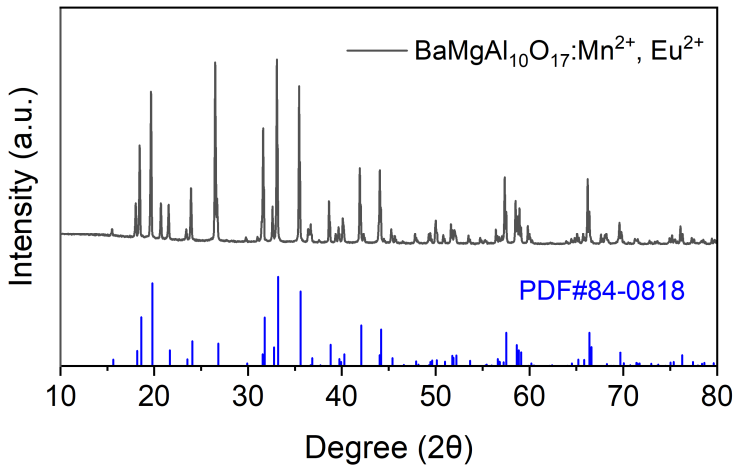

Figure S15. X-ray diffraction patterns of UV excited phosphor.

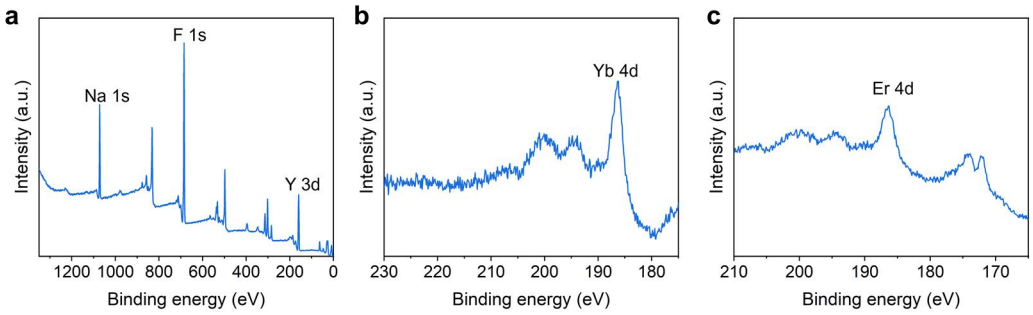

Figure S16. XPS spectra of NIR excited phosphor.

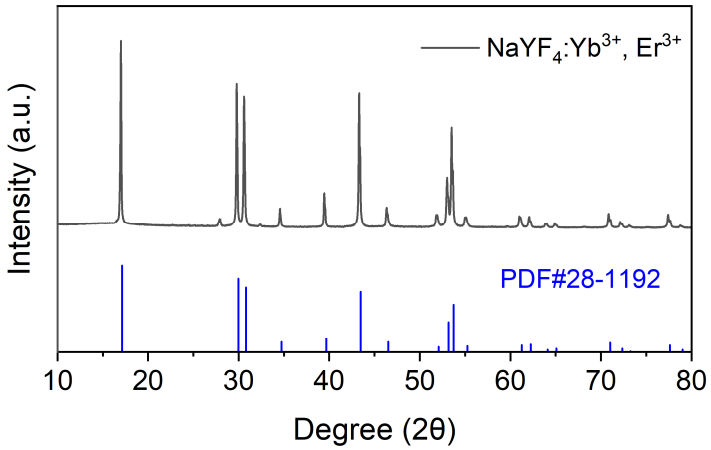

Figure S17. X-ray diffraction patterns of NIR excited phosphor.

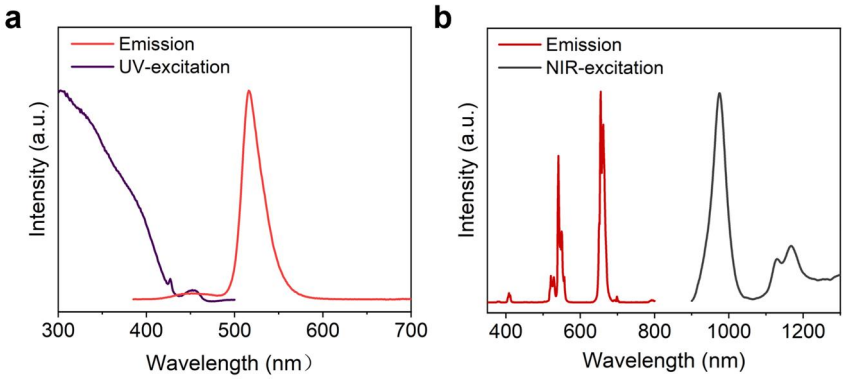

Figure S18. a) Excitation and emission curves of the used UV excited phosphor, showing a quantum yield of 80.94% at λ_{ex} = 365 nm. Upon excitation at 365 nm, the phosphor exhibits two emission bands centered at 450 and 510 nm, which can be attributed to $4f^6 5d \rightarrow 4f^7 ({}^8S_{7/2})$ transition of Eu^{2+} and ${}^4T_1 \rightarrow {}^6A_1$ transition of Mn^{2+}, respectively.[54, 55] b) Excitation and emission curves of the used NIR excited phosphor, showing a quantum yield of 83.75% at λ_{ex} = 980 nm. Upon excitation at 980 nm, the phosphor exhibited characteristic sharp emission peaks, which can be attributed to ${}^2H_{9/2} \rightarrow {}^4I_{15/2}$, ${}^2H_{11/2} \rightarrow {}^4I_{15/2}$, ${}^4S_{3/2} \rightarrow {}^4I_{15/2}$ and ${}^4F_{9/2} \rightarrow {}^4I_{15/2}$ transitions of Er^{3+}.[56, 57]

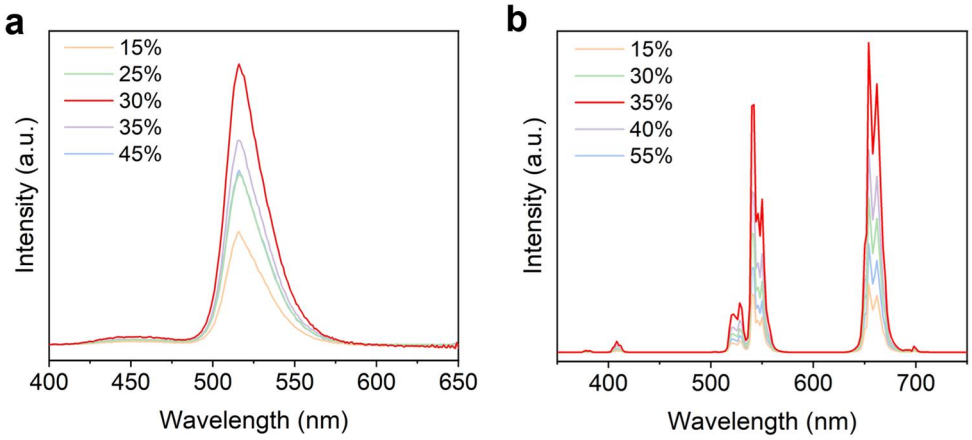

Figure S19. a) Photoluminescence emission intensities of light conversion layers containing different contents of UV excited phosphors, exhibiting the highest emission intensity with the phosphor content of 30%. b) Photoluminescence emission intensities of light conversion layer containing different contents of NIR excited phosphors, showing the highest emission intensity with the phosphor content of 35%.

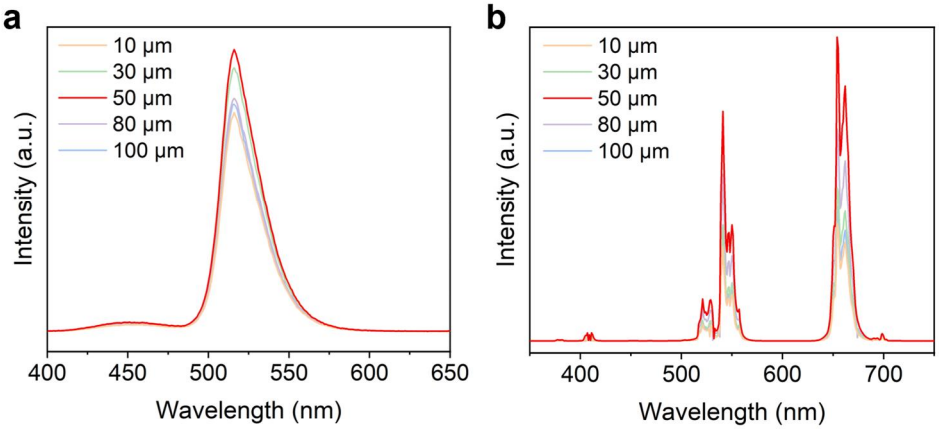

Figure S20. a, b) Photoluminescence emission intensities of light conversion layers with different thicknesses excited by UV and NIR light, respectively.

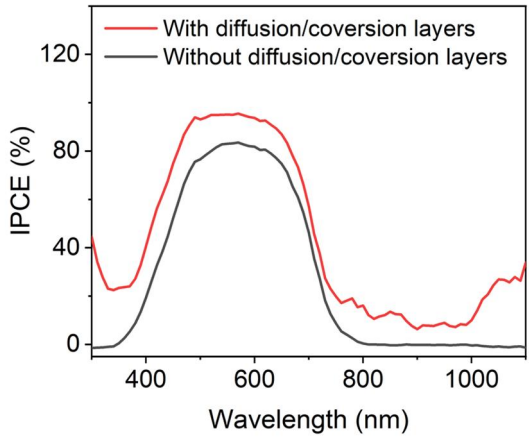

Figure S21. IPCE spectra of FDSSCs with and without diffusion/conversion layers, showing the highest IPCE values of 95.52% and 83.54% at 520 nm, respectively. The FDSSC with diffusion/conversion layer showed obviously widened spectral range and increased photogenerated electrons, demonstrating its remarkably enhanced light harvesting. In 300−1100 nm wavelength range, the conversion efficiencies when converting UV and NIR light into wavelengths that overlap with the absorption spectrum of the active N719 dye were 27.92% and 13.18%, respectively.

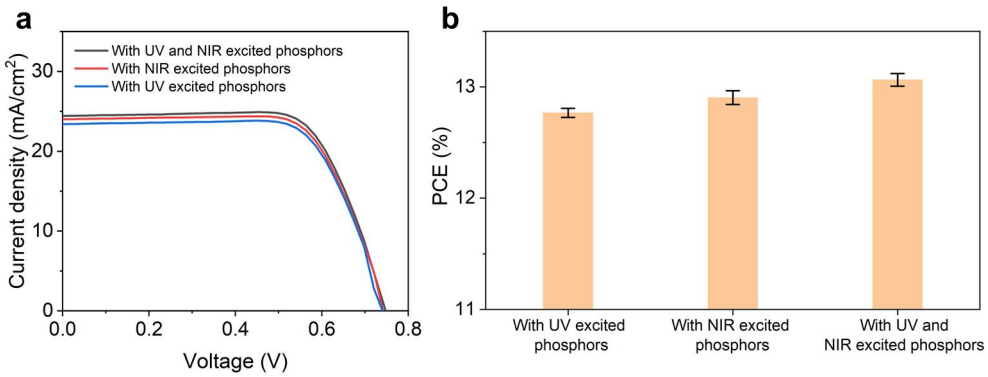

Figure S22. a) *J-V* curves of FDSSCs with different phosphors. The PCE of FDSSC with UV excited phosphors was 12.76%, with a J_{SC} of 24.013 mA/cm^2, a V_{OC} of 0.745 V, and an FF of 0.713. The PCE of FDSSC with NIR excited phosphors was 12.92%, with a J_{SC} of 24.324 mA/cm^2, a V_{OC} of 0.753 V, and an FF of 0.710. The PCE of FDSSC with both UV and NIR excited phosphors was 13.11%, with a J_{SC} of 24.433 mA/cm^2, a V_{OC} of 0.755 V, and an FF of 0.710. b) PCE values of FDSSCs using light conversion layers with different phosphors. Error bars, standard deviations of the results from five samples. Compared to UV excited phosphors, NIR excited phosphors can achieve a higher conversion efficiency and therefore produce higher current. With synergetic use of both UV and NIR excited phosphors, the current of FDSSC could be further improved with the highest PCE.

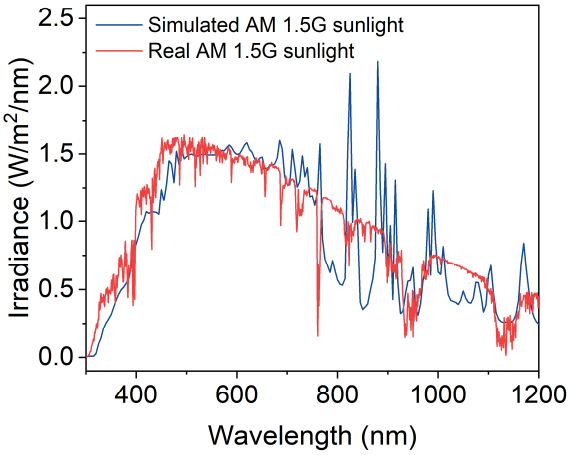

Figure S23. Spectra of simulated and real AM 1.5G sunlight. The simulated solar spectrum showed a high spectral matching degree with the real sunlight, which met the international AAA standard (IEC 60904-9, JIS 8904-9, ASTM E927-10).

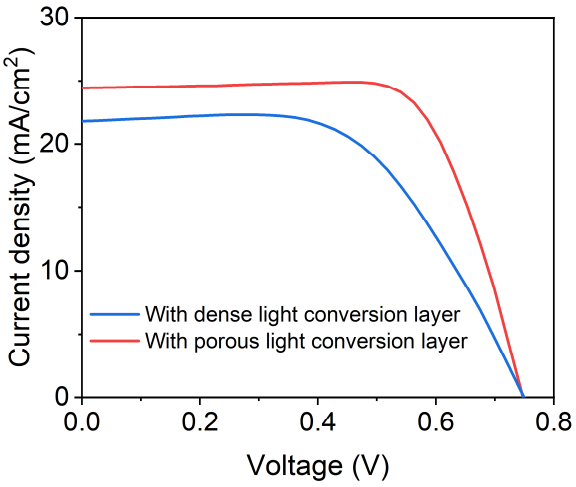

Figure S24. *J-V* curves of FDSSCs with dense and porous light conversion layers. The PCE of FDSSC with porous light conversion layers was 13.11%, with a J_{SC} of 24.433 mA/cm^2, a V_{OC} of 0.755 V, and an FF of 0.710. In contrast, the FDSSC with dense light conversion layers showed a much lower PCE of 9.43%, with a J_{SC} of 21.80 mA/cm^2, a V_{OC} of 0.750 V, and an FF of 0.580. The much higher impendence of the counter electrode covered with a dense layer caused severe charge recombination and seriously decreased J_{SC} and FF.

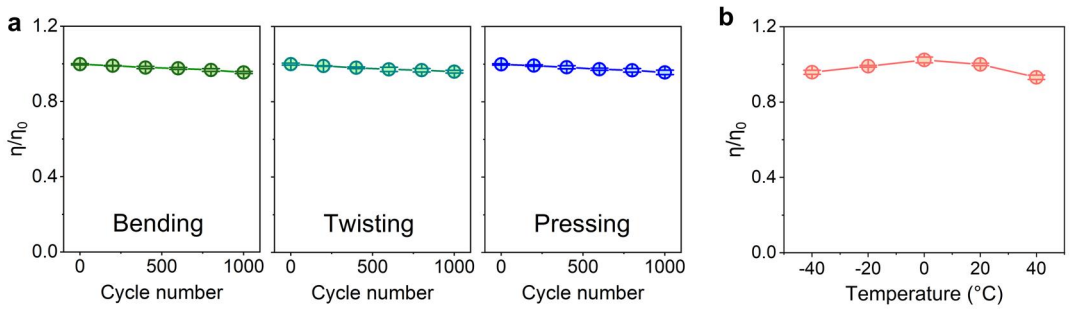

Figure S25. a) Mechanical stability of FDSSCs against bending, twisting, and pressing. Error bars, standard deviations of the results from five samples. The PCEs were maintained by over 90% after 1,000 cycles for each deformation mode. b) Stability of FDSSCs at temperatures of −40 °C to 40 °C, showing PCE variations of less than 10%. Error bars, standard deviations of the results from five samples.

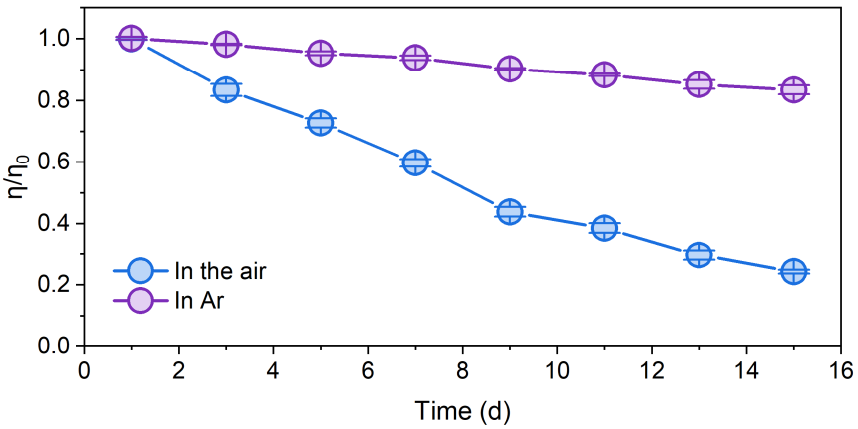

Figure S26. Long-term stability of FDSSCs under outdoor solar exposure. They were placed in a sealed glass box that can be filled with argon, showing PCE variations of less than 20% in argon condition after 15 days. The larger performance variations in air condition indicated the needs to improve flexible encapsulating materials and technologies. Error bars, standard deviations of the results from five samples.

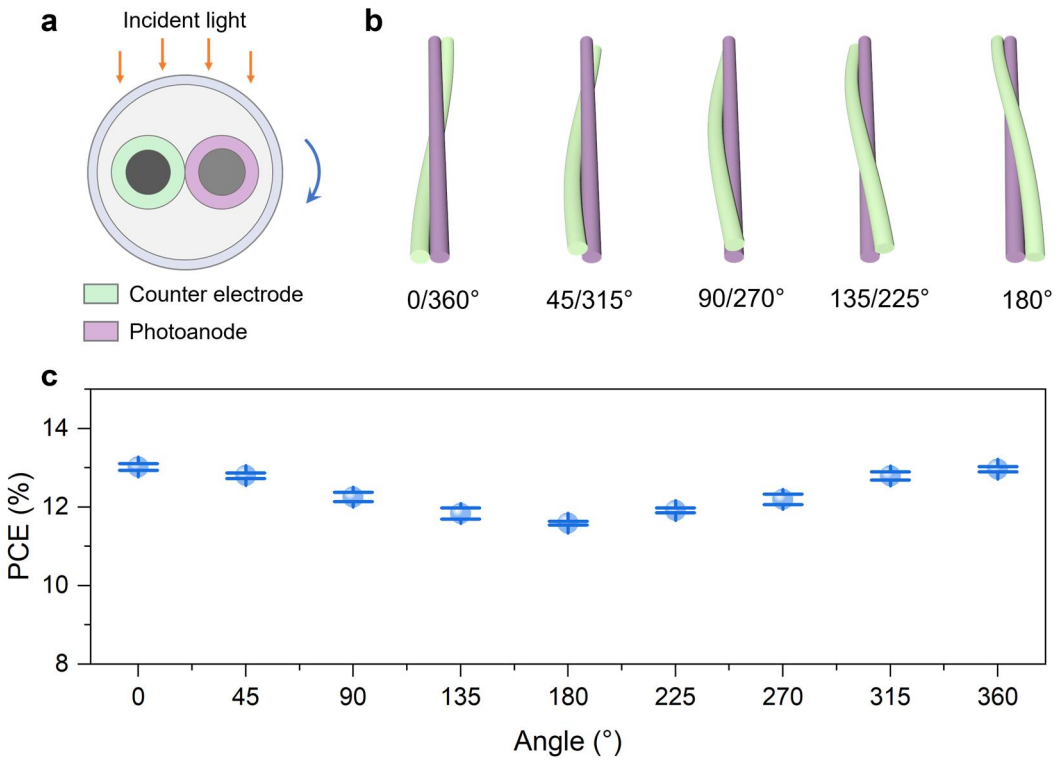

Figure S27. a) Schematic cross-sectional diagram of the FDSSC under incident light. b) Schematics illustrating the top views of FDSSCs placed with different angles under the incident light to explore their PCE dependency on the incident light direction. c) Corresponding photovoltaic performances of FDSSCs placed with different angles. The PCEs of FDSSCs had been maintained by over 90% under the incident light from different directions. Error bars, standard deviations of the results from five samples.

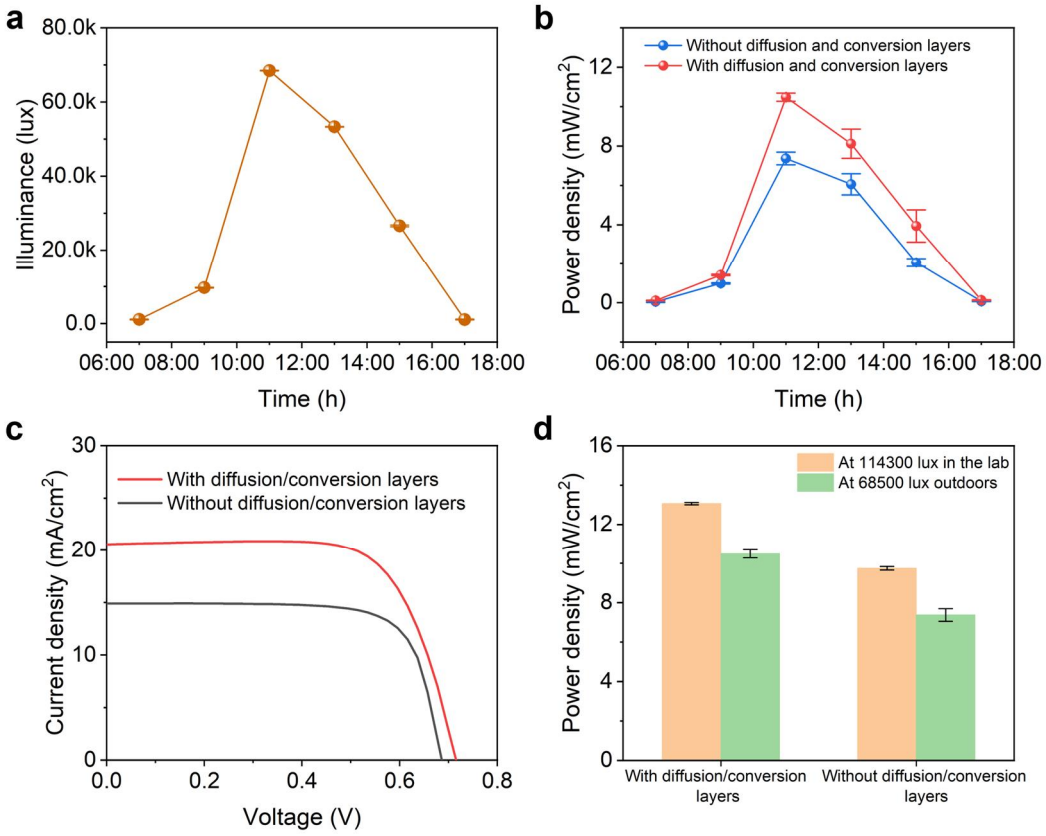

Figure S28. a) The illuminances of sunlight at different time during one day. b) Power densities of FDSSCs without and with light diffusion and conversion layers under outdoor sunlight at different time during one day. c) *J*-*V* curves of FDSSCs without and with light diffusion and conversion layers measured under 68500 lux illumination of outdoor sunlight. d) Power densities of FDSSCs without and with light diffusion and conversion layers under 68500 lux illumination of outdoor sunlight and 114300 lux illumination of simulated AM 1.5G light. Error bars, standard deviations of the results from five samples.

Figure S29. Photograph of pigments with different colors.

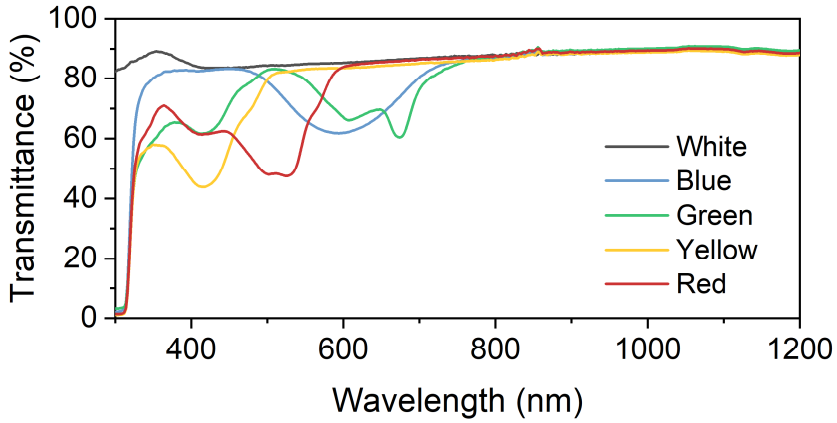

Figure S30. Transmittance spectra of light diffusion layers with different colors.

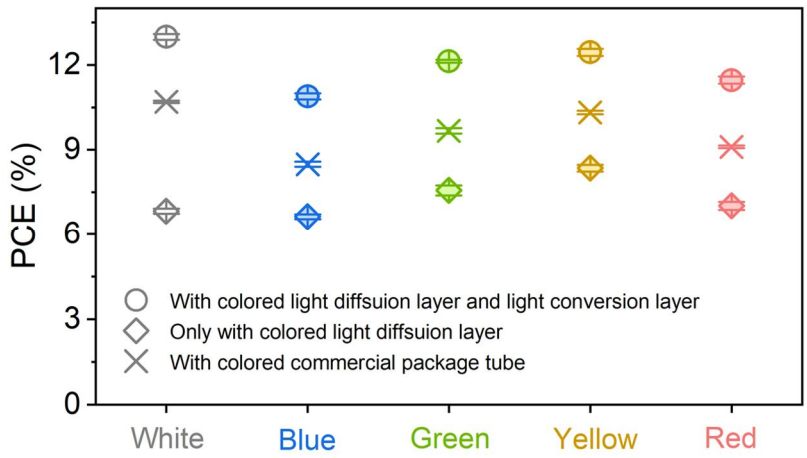

Figure S31. PCE values of different types of multicolored FDSSCs. Error bars, standard deviations of the results from five samples.

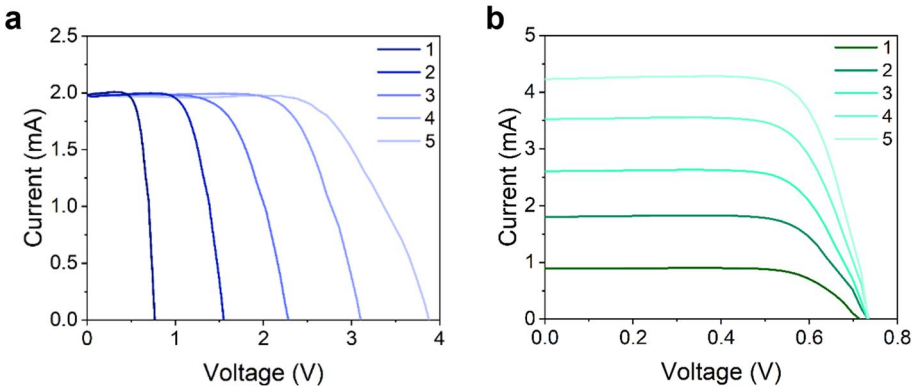

Figure S32. a, b) *I-V* curves of FDSSCs connected in series and in parallel, respectively.

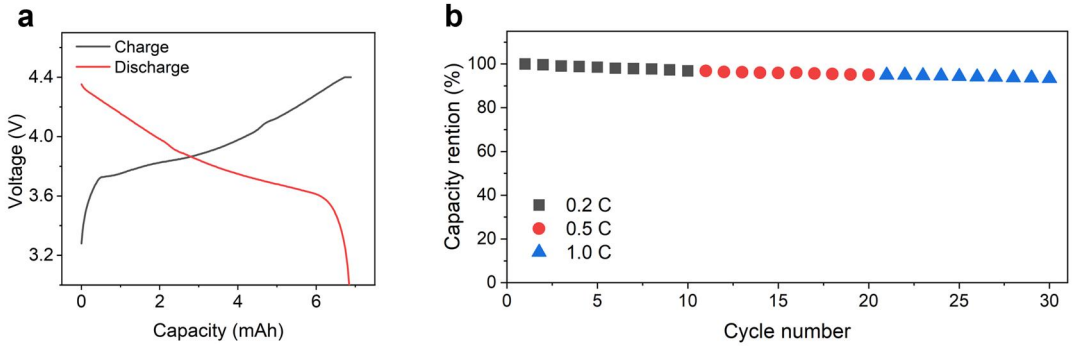

Figure S33. a) Typical charge and discharge profiles of a fiber lithium-ion battery. The fiber lithium-ion battery was charged from 3.0 to 4.4 V at 0.2 C rate, and subsequently discharged to 3.0 V at 0.5 C rate, showing a capacity of 6.8 mAh. b) Cycling stability of the fiber lithium-ion battery.

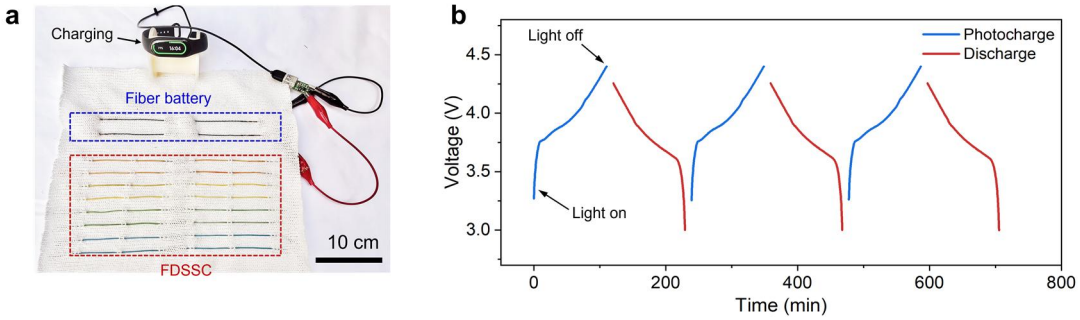

Figure S34. a) Photograph of a textile integrated with FDSSCs and fiber lithium-ion batteries to power a smart bracelet. b) Photocharge/discharge curves of self-charging power system. A fiber lithium-ion battery with a capacity of 6.8 mAh was charged from 3.0 to 4.4 V by FDSSCs under simulated AM 1.5G sunlight and then discharged to 3.0 V at 0.5 C rate.

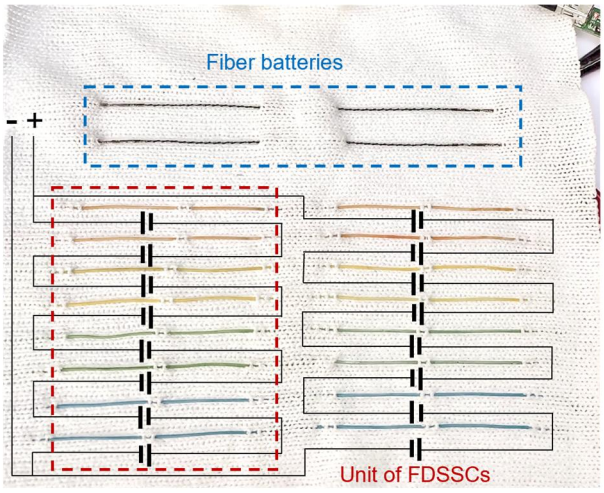

Figure S35. Photograph of FDSSC modules illustrating their electrical connection in series and in parallel. A unit in photovoltaic modules was composed of 8 FDSSCs connected in series for appropriate voltage, and then two units were connected in parallel for increased photocurrent. The leading wires of photovoltaic modules were further connected with the positive and negative anodes of fiber lithium-ion batteries.

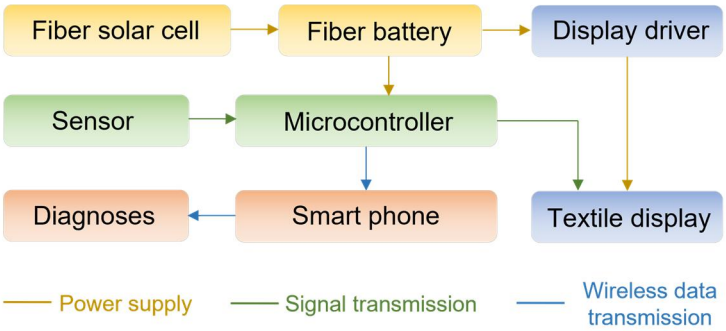

Figure S36. Diagram showing the integration design of smart garment. Health monitoring and displaying modules were powered by power-supplying textile.

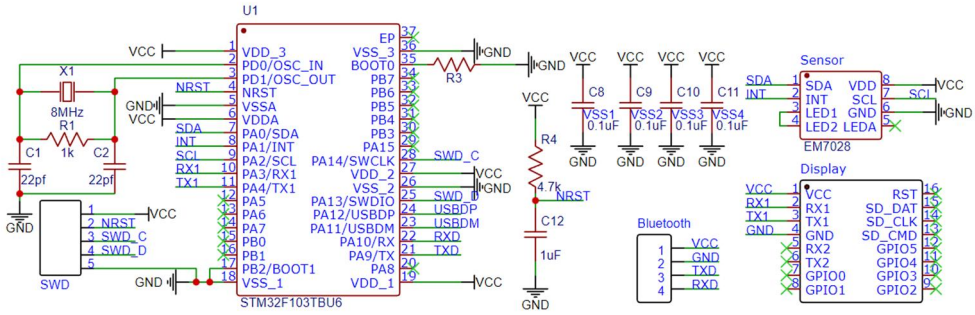

Figure S37. Schematic of the circuit design for the integrated textile system.

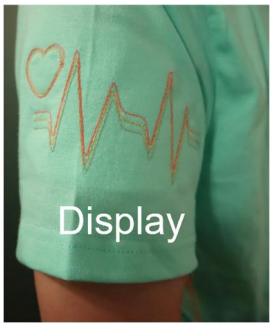

Figure S38. Photograph showing textile display on the right arm powered by FDSSCs and fiber lithium-ion batteries, acting as an indicator of heart rate status.

Table S1. EIS data in Figure S9.

	R_S ($\Omega \cdot cm^2$)	R_{CT} ($\Omega \cdot cm^2$)	Z_N ($\Omega \cdot cm^2$)
Without light conversion layer	1.76	0.30	33.40
With dense light conversion layer	4.43	0.63	144.71
With porous light conversion layer	4.53	0.73	45.99

Table S2. Photovoltaic parameters of the FDSSCs in Figure S12b.

Content (%)	V_{OC} (V)	J_{SC} (mA/cm^2)	FF	PCE (%)
0	0.735	17.730	0.755	9.840
5	0.735	18.313	0.751	10.106
10	**0.739**	**19.215**	**0.758**	**10.711**
15	0.733	16.708	0.759	9.301
20	0.732	15.296	0.754	8.439

Table S3. Photovoltaic parameters of the FDSSCs in Figure 4d.

Color	V_{OC} (V)	J_{SC} (mA/cm^2)	FF	PCE (%)
White	0.755	24.433	0.710	13.110
Yellow	0.750	23.520	0.706	12.453
Green	0.750	23.200	0.700	12.125
Red	0.751	21.079	0.719	11.373
Blue	0.749	20.777	0.701	10.897

Supplementary References

[48] Y. Fu, H. Wu, S. Ye, X. Cai, X. Yu, S. Hou, H. Kafafy, D. Zou, *Energy Environ. Sci.* **2013**, 6, 805.

[49] M. R. Lee, R. D. Eckert, K. Forberich, G. Dennler, C. J. Brabec, R. A. Gaudiana, *Science* **2009**, 324, 232.

[50] Y. Fu, Z. Lv, S. Hou, H. Wu, D. Wang, C. Zhang, Z. Chu, X. Cai, X. Fan, Z. L. Wang, D. Zou, *Energy Environ. Sci.* **2011**, 4, 3379.

[51] L. Porrès, A. Holland, L.-O. Pålsson, A. P. Monkman, C. Kemp, A. Beeby, *J. Fluores.* **2006**, 16, 267.

[52] L. O. Pålsson, A. P. Monkman, *Adv. Mater.* **2002**, 14, 757.

[53] J. C. de Mello, H. F. Wittmann, R. H. Friend, *Adv. Mater.* **1997**, 9, 230.

[54] Y. Liu, C. Shi, *Mater. Res. Bull.* **2001**, 36, 109.

[55] P. Yang, G. Yao, J. Lin, *Opt. Mater.* **2004**, 26, 327.

[56] F. Wang, X. Liu, *J. Am. Chem. Soc.* **2008**, 130, 5642.

[57] M. Ding, S. Yin, D. Chen, J. Zhong, Y. Ni, C. Lu, Z. Xu, Z. Ji, *Appl. Surf. Sci.* **2015**, 333, 23.